PHYSICAL REVIEW B **98**, 235431 (2018)

Strong in- and out-of-plane excitons in two-dimensional InN nanosheets

Maria Stella Prete and Olivia Pulci
Dipartimento di Fisica, and INFN, Università di Roma Tor Vergata, Via della Ricerca Scientifica 1, I-00133 Rome, Italy

Friedhelm Bechstedt
IFTO, Friedrich-Schiller-Universität and ETSF, Max-Wien-Platz 1, 07743 Jena, Germany

(Received 5 July 2018; revised manuscript received 17 October 2018; published 27 December 2018)

Using density-functional and many-body perturbation theory, we study the electronic, optical, and excitonic properties of indium nitride as single monolayer and bilayer in comparison with the bulk phase. We investigate the stable geometry for the monolayer, the graphenelike unbuckled honeycomb structure, and for the bilayer the AA' stacking geometry. We demonstrate that the quasiparticle and optical gaps, going from bulk to two-dimensional systems, open dramatically due to strong quantum confinement and reduced screening. Large excitonic effects, which survive at room temperature, are predicted. Our results suggest that low-dimensional InN is a promising material for optoelectronic devices in the visible to near-infrared spectral ranges varying with the number of atomic layers and light propagation.

DOI: 10.1103/PhysRevB.98.235431

I. INTRODUCTION

A great deal of attention and research efforts have been devoted in the last years toward the study of quantum confinement of electrons in two-dimensional (2D) sheets [1–3], such as graphene, MoS_2, 2D BN, topological insulators, and 2D superconductors [4]. Reduced dimensionality enhances quasiparticle (QP) and excitonic effects, and dramatically shapes the electronic and optical properties of these materials.

Bulk group-III mononitrides AlN, GaN, and InN are the most important materials for solid-state lighting [5] and solar cells [6]. Consequently, increasing interest arises in 2D nitrides, although the strong bulk sp^3 bonding makes their preparation extremely difficult. Only 2D BN is easily obtained by exfoliation of hexagonal BN and has been proven to be an attractive substrate for graphene [7]. Experimentally, successful attempts to obtain 2D AlN [8] and 2D GaN [9] pave the way to photovoltaic and optical nanodevices based on 2D nitrides. Theoretical studies on the tunable electronic gap of group-III nitrides and alloys have appeared [10–12], suggesting these materials as building blocks for light harvesting devices. *Ab initio* calculations of optical properties of freestanding 2D GaN predict an optical gap of about 5 eV for 1 ML, and 3.3 eV for 2 ML, hence in both cases an emission in the UV spectral range [13]. 2D GaN embedded in AlN has also been studied [14]. Measurements of GaN sheets encapsulated by graphene seem to confirm a fundamental gap of about 5 eV [15]. Heterocombinations of AlN and GaN sheets with MoS_2 monolayers have been suggested to be efficient water-splitting devices [16]. In the bulk case, a central tool for band-gap engineering is the alloying of GaN with InN. The use of InN in alloys with GaN and/or AlN makes it possible to extend the emission of nitride-based LEDs from ultraviolet to visible and near-infrared regions [17,18].

In contrast to 2D AlN and GaN, much less is known about 2D InN. In its bulk form, it crystallizes in wurtzite (WZ) and zinc-blende (ZB) structures, the first one being the most stable phase, with a direct band gap of about 0.7 eV [19]. Moreover, bulk InN possesses the smallest effective mass for electrons in all the III-nitride semiconductors [20], which leads to high electron mobility and high saturation velocity, thus enabling InN to be a promising material not only for light emission but also for high-speed and high-frequency electronic devices [21]. Consequently, various InN nanostructures have been tried to synthesize [22,23]. Theoretically, the InN monolayer has been verified to possess thermal stability, high-carrier mobility, large drift velocity, strong light absorption, and sizable band gap [11,24–26]. Unlike graphenelike group-IV materials, monolayer InN is a semiconductor with a considerable band gap [11,26,27] that can be tuned by alloying [11,28] or heterostructuring [25]. Other modifications of the electronic properties are possible by adsorption of gas molecules [29].

Bulk InN crystals grown in WZ or ZB structures possess a small but finite direct band gap of the order of 0.7 eV [20]. Its theoretical treatment is, however, difficult [30]. The In $4d$ electrons have to be taken into account to obtain the correct lattice constants minimizing the total energy obtained in the framework of the density-functional theory (DFT) [31]. The treatment of exchange and correlation (XC) within the local density approximation (LDA) or the generalized gradient approximation (GGA) [32] gives, however, rise to negative Kohn-Sham energy gaps. This tendency is enforced by the p-d repulsion shifting the valence band maximum (VBM) toward higher energies [30]. Only self-interaction-corrected or relaxation-corrected pseudopotentials allow us to open a small gap [33]. The description of the self-interaction and the local XC for electrons with spatially localized wave functions by an additional Hubbard U term may indeed open the bulk InN gap [34,35]. However, the application of DFT+U methods on 2D crystals such as atomic layers of InN has not been studied until now.

2469-9950/2018/98(23)/235431(9)

Here, we investigate the electronic and optical properties of single layer (g-InN) and bilayer (b-InN) indium nitride. We predict that, with reduced dimensionality, the fundamental electronic gaps are direct, the electron mass is extremely small, and that quantum confinement opens the electronic gap up to 1.7 eV for g-InN, and 0.86 eV for b-InN. Strong excitonic effects appear, with binding energies much larger than the thermal energy $k_B T$ at room temperature, thus suggesting the possibility to use 2D InN in optical nanodevices in the near-infrared or visible spectral range.

II. METHODS

First-principles calculations are performed to investigate the properties of bulk InN, single-layer InN, and bilayer InN. We use DFT with an XC LDA functional and norm-conserving pseudopotentials to describe structural and electronic properties as implemented in the PWSCF package of Quantum ESPRESSO code [36]. The kinetic energy cutoff of the plane-wave basis set is taken as 100 Ry. Shifted $4 \times 4 \times 4$, $5 \times 5 \times 5$ **k**-point meshes were employed for the self-consistent calculations for ZB and WZ geometries, respectively. For g-InN and b-InN, we used a shifted $12 \times 12 \times 1$ **k**-point mesh. To avoid spurious interactions between the periodic images, supercells with at least 21 Å vacuum space are adopted for the 2D InN (the vacuum was decreased to 15 Å in the subsequent QP calculations). The In 4d electrons are treated as valence electrons for a correct description of the geometry and electronic structure of the material [37]. To take into account van der Waals (vdW) interaction in the bilayer structure, we also perform calculations using XC based on the Perdew-Burke-Ernzerhof (PBE) [38] functional but including vdW corrections [39].

Since DFT is a ground-state theory, the excitation aspect is missing. Therefore, in the electronic band-structure calculations, many-body QP effects have to be included within the GW method, with G single particle Green's function and W screened Coulomb potential [40]. Since, however, bulk InN possesses a negative gap in LDA and PBE calculations for both polytypes, WZ and ZB [41], the one-shot G_0W_0 approach cannot be applied in bulk InN. One possibility is to open a small gap by self-interaction corrections described by Hubbard U parameters (see below) to generate a gapped starting electronic structure for the G_0W_0 treatment [41]. Here, we determine the U parameter for bulk InN, and apply the very same U values also for 2D InN, as an approximated way to take into account QP effects. Then, we compare our results with those obtained with the more appropriate G_0W_0 approach.

Our G_0W_0 calculations on 2D InN are performed with the CHISIG code [42] using, for the exchange part of the self-energy, $102 \times 102 \times 1$ **k**-point mesh centered on Γ in the Brillouin Zone (BZ), and 16 000 and 45 000 plane waves for g-InN and b-InN, respectively. For the correlation self-energy and for the screened Coulomb interaction W we have used $51 \times 51 \times 1$ **k**-point meshes and 4000 plane waves for g-InN and $39 \times 39 \times 1$ **k**-point meshes and 7000 plane waves for b-InN. The total number of bands used is 300 for both configurations. We have used the plasmon-pole approximation for W and the spurious interactions between adjacent supercells have been treated by cutting the Coulomb potential along z (z being the normal to the sheet material) [43].

The optical properties of a bulk semiconductor, and especially its nanostructures, ask for the inclusion of excitonic effects by solving the Bethe-Salpeter equation (BSE) for the polarization function [40,44]. Whereas bulk bound exciton states possess only very small exciton binding energies (about 5 meV [34]), the binding energies are much larger in 2D crystals (see, e.g., Ref. [45]). For 2D InN, we made the extremely accurate BSE calculations as implemented in the DP4EXC code [46], using 595 plane waves (795 for b-InN) to describe the wave functions and 205 (291 for b-InN) reciprocal lattice vectors for the screening matrix in W. Since we are interested in the absorption spectra until 10 eV, it is sufficient to include the three highest valence bands and five lowest conduction bands for InN and the six highest valence bands and six lowest conduction bands for b-InN. BSE is solved using the Tamm-Dancoff approximation. For a better understanding of the mechanism and the screening of the electron-hole interaction, we also investigate excitonic effects through a variational scheme applied to a simple model Hamiltonian that describes the interaction of electrons and holes in a homogeneous 2D sheet [47–49].

III. BULK

In bulk InN, the DFT-LDA approach significantly underestimates the electronic band gap and fails in predicting the symmetry of the states close to the top of the valence bands. The band structures in Figs. 1(a) and 1(b) show inverted bands and, hence, a zero or "negative" gap for both ZB and WZ crystals. The s-like Γ_{1c} states are below the predominantly p-like Γ_{15v} (Γ_{6v} and Γ_{1v}) bands for ZB (WZ) neglecting spin-orbit interaction. The main reason is the overestimation of the $p-d$ repulsion with the localized In 4d electrons, which, however, are much too high in energy in DFT-LDA [41]. As a result, the VBM is pushed toward higher energies, thus closing the gap.

A computational efficient way to solve the band-ordering problem is based on the Hubbard LDA+U method, where the U parameter takes better care of correlation effects. Usually, only a Hubbard interaction is taken into account for localized d electrons, which, however, opens gap that is too small (see Ref. [41]). Therefore, as suggested in the literature [50], besides the interaction U_d on the In 4d states, we also allow an interaction U_p among the N 2p states. We systematically varied both U_p and U_d by considering the correlation effects on the In 4d bands and on the fundamental gap at Γ. Using $U_p = 3.5$ eV and $U_d = 6.5$ eV, we obtain a gap of 0.61 eV for ZB and of 0.8 eV for WZ [Figs. 1(c) and 1(d)] in agreement with experimental data [19] (see also collection in Ref. [20]). Moreover, the position of 4d states of indium are now about 16 eV below the VBM, in agreement with the experiments [35]. The N 2s states lay 12 eV in the WZ structure and at 13.5 eV in the cubic phase below the VBM. Applying the U_p and U_d corrections, the right symmetry of the band states close to the fundamental gap is also recovered. The resulting fundamental gaps in Figs. 1(c) and 1(d) are close to those derived within GW calculations [20]. Therefore, the LDA+U band structures can be interpreted as approximate QP band structures. The described LDA+U approach is also used in the following for the 2D InN systems, and compared with the results obtained within the G_0W_0 approach.

IV. MONOLAYER (g-InN)

A flat, unbuckled honeycomb structure is the most stable geometry for one atomic layer of InN [25,26]. For this pristine structure, our LDA calculations give a lattice constant $a = 3.52$ Å and an In-N bond length $d = 2.03$ Å, in agreement with other DFT studies [11,25,26]. In PBE, our lattice constant results to be 3.61 Å, indicating the reduced bonding strength after inclusion of gradient corrections [40]. We find that the cohesive energy for *g*-InN is 1.12 eV/pair lower than the WZ InN bulk one. Hence, although the graphenelike geometry represents a local minimum on the energy landscape, the higher cohesive energy shows that freestanding *g*-InN is a metastable configuration.

The electronic band structure in Fig. 2(a), calculated within DFT-LDA, shows a 0.80 eV $\Gamma - \Gamma$ direct gap and an almost degenerate 0.81 eV $K - \Gamma$ indirect gap. The presence of a gap already at the DFT level is at odd with the findings in the bulk. No inversion of the character of the bands occurs at Γ. The top of the valence band results to have *p* (84% of N and 10% of In) character, whereas the bottom of the conduction band possesses mainly *s* (60% In and 23% N) character. The lack of band inversion suggests that, despite the wrong position of the *d* states as in bulk, it has a minor influence on the *p* states because the quantum confinement effects are so strong that they partially counterbalance the shrinking, hence preventing the closing of the gap. Of course, XC effects calculated at the LDA level still cause an energy-band-gap underestimation, that has to be cured through the introduction of QP effects within the G_0W_0 method. The results of our LDA+G_0W_0 are displayed in Fig. 2(c). The electronic gaps open about 0.9–1.2 eV. Interestingly, the almost complete degeneracy (at the DFT-LDA level) of the $\Gamma - \Gamma$ and $K - \Gamma$ gaps is lifted. The resulting fundamental gap of *g*-InN is direct, at $\Gamma - \Gamma$, and measures 1.72 eV (see Table I), while the indirect gap amounts to 2.05 eV.

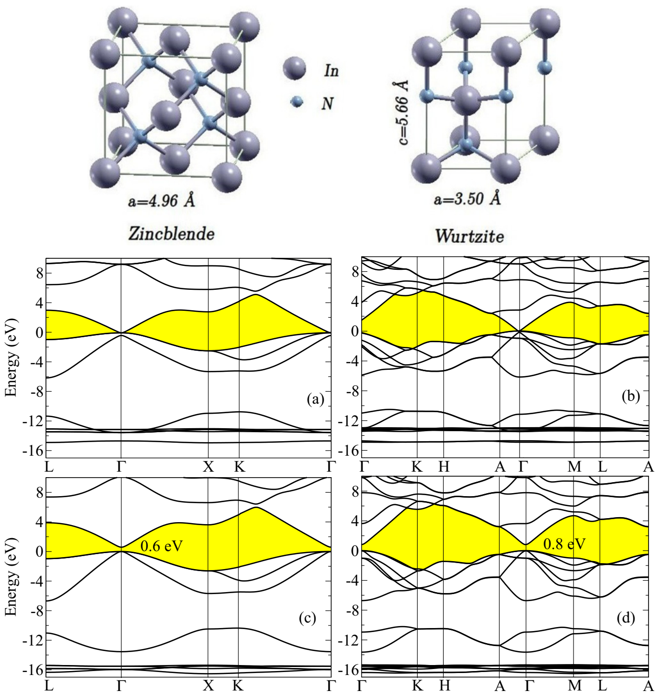

FIG. 1. Equilibrium structures of ZB InN and WZ InN. Lattice parameters are indicated. Large (grey) and small (blue) balls denote In and N atoms, respectively. Band structures of ZB InN (a), (c) and WZ InN (b), (d) are, calculated within LDA (left) and LDA+U (right) approximations. The fundamental gap region is shown in yellow.

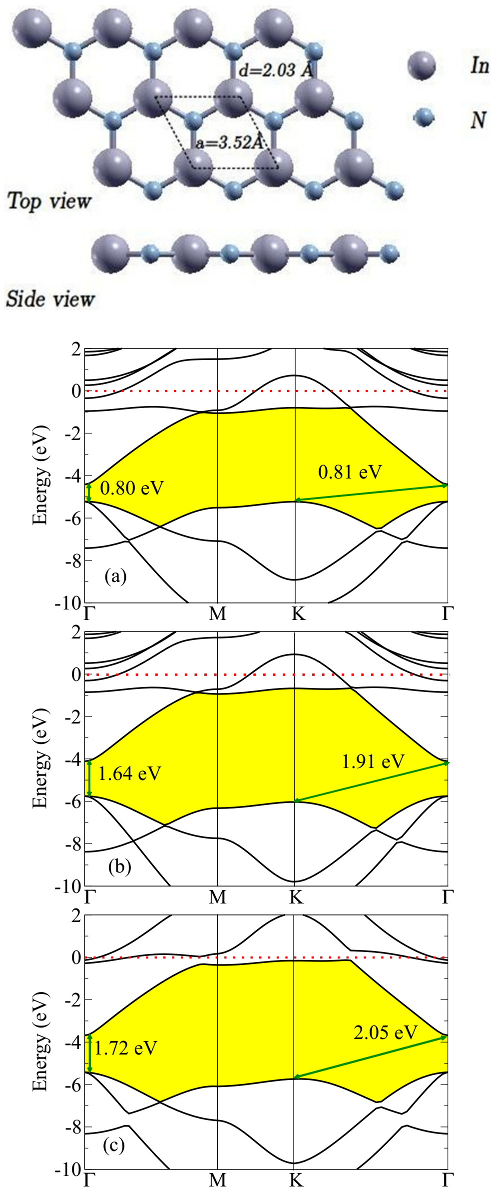

FIG. 2. Top and side views of the optimized hexagonal atomic structure of *g*-InN. The 2D primitive unit cell is indicated by dashed lines. The lattice constant *a* and the In-N bond length *d* are indicated. Large (grey) and small (blue) balls denote In and N atoms, respectively. Electronic band structure of *g*-InN calculated within LDA (a), LDA+U (b), and within G_0W_0 approach (c). The vacuum level, identified with the energy zero, is shown as red dotted horizontal line.

TABLE I. *Ab initio* electronic (GW) and optical (BSE) gaps for monolayer and bilayer InN. Also the *ab initio* excitonic binding energies are reported. All values are in eV.

geometry	GW gap	BSE gap	E_b^{exc}
g-InN	1.72 eV (ΓΓ)	1.17 eV	0.55 eV
b-InN (AA')	0.86 eV (ΓΓ)	0.42 eV	0.44 eV

Our results are in rough agreement with other LDA+G_0W_0 calculations [25]. However, they are in contrast to the results in Ref. [26], where QP effects are significantly overestimated, and to another *ab initio* study [27] that presents results within the hybrid HSE06 functional [51] and a partly self-consistent GW_0 calculation based on Kohn-Sham computations using the semilocal XC PBE potential [38]. In particular, a first small effect on the gap discrepancies is due to the difference in the computed lattice constants, ours being 1.4% shorter in the LDA case [26] and 0.6% in the GGA limit [27]. Regarding results in Ref. [27], already at DFT level the results are not in agreement. In fact, a much smaller indirect DFT-PBE gap $E_{K\Gamma} = 0.31$ eV compared to our DFT-LDA values of $E_{K\Gamma} = 0.81$ eV and $E_{\Gamma\Gamma} = 0.80$ eV is used in the starting electronic structure. The main reason for the different DFT results is the different lattice constant. The equilibrium structure in Ref. [27] is characterized by $a = 3.63$ Å (PBE), while we obtained $a = 3.52$ Å (LDA). We repeated the DFT-LDA band-structure calculations at the larger PBE lattice constant, i.e., for a tensile biaxial strain of 3.1%, and found an indirect gap of $E_{\mathrm{ind}} = 0.33$ eV in agreement with the DFT-PBE result. The huge lattice-constant influence is an indication for a supersensitivity of the electronic structure of an InN monolayer to (biaxial) strain. Comparing biaxially strained and unstrained gap data, we computed biaxial gap deformation potentials of $D_{\mathrm{dir}} = -15.2$ eV and $D_{\mathrm{ind}} = -15.5$ eV within DFT-LDA. These deformation potentials are larger than the volume deformation potentials of direct gaps in bulk semiconductors [52].

However, more important for the gaps are the various approximate descriptions of the QP gap openings. Apart from the deviating numerical details and the partly self-consistent GW_0 QP calculations in Ref. [27], the most important difference lies in the fact that from their calculations for *g*-InN, it turns out that the VBM occurs at the *K* point, whereas the conduction band minimum (CBM) appears at the Γ point. The corresponding indirect $K - \Gamma$ gaps are $E_{K\Gamma}^{\mathrm{HSE06}} = 1.48$ eV and $E_{K\Gamma}^{\mathrm{GW}_0} = 2.02$ eV, respectively. Discussing the optical absorption, the authors in Ref. [27] speak about a QP direct $\Gamma - \Gamma$ gap of 2.02 eV. Obviously, they found an indirect QP gap of the same size, in contrast to our finding of a direct semiconductor with a $\Gamma - \Gamma$ QP gap of $E_{\Gamma\Gamma} = 1.72$ eV.

In addition, we also applied the approximate QP LDA+U method to the *g*-InN system, using the same U parameters as for the 3D bulk InN structures to compare it with our result obtained with the suitable G_0W_0 calculation. The resulting band structure is shown in Fig. 2(b). The direct gap increases to 1.64 eV, while the indirect gap is about 1.91 eV. Hence, also in LDA+U we find a direct gap for *g*-InN.

We notice that the LDA+U gap values are close to G_0W_0 results in Fig. 2(c). The only 0.1 eV underestimate of the gaps suggests that almost the same U employed for 3D structures can be used to predict the electronic properties of low-dimensional InN geometries. In other words, thanks to the quantum confinement, correlation effects related to localized N 2*p* and In 4*d* electrons are already well described at the DFT-LDA level (in the sense that the inversion of the bands and the closure of the gap do not occur), and the role of U is mainly to correct that part of correlation that is independent of the dimensionality of the system.

In the band structures in Fig. 2, the vacuum level is set as zero energy. It has been derived from the electrostatic part of the single-particle Kohn-Sham potential. The differences to the VBM and CBM define the ionization energy I and the electron affinity A, respectively. They are $I = 5.42$ eV (5.71 eV, 5.16 eV) and $A = 3.70$ eV (4.06 eV, 4.36 eV) eV within the LDA+G_0W_0 (LDA+U, LDA) approximation. The curvatures of the uppermost valence band and the lowest conduction band at the band extrema at Γ characterize the effective electron and hole masses m_e^* and m_h^*, respectively. As listed in Table III, the masses indicate very light electrons and light holes with $m_e^* = 0.083\, m$ and $m_h^* = 0.43\, m$.

Optical properties of *g*-InN have been studied at three different levels of the theory: within the independent-particle approach (IPA), within the independent-QP approach at the G_0W_0 level, and also with the inclusion of excitonic effects by solving the BSE to account for the electron-hole coupling. In Fig. 3, we present the polarization-dependent optical conductivity calculated within G_0W_0 and within BSE, together with the G_0W_0 interband structure, $\Delta\epsilon_{cv}(\mathbf{k}) = \epsilon_c(\mathbf{k}) - \epsilon_v(\mathbf{k})$ with the corresponding conduction (valence) band energy $\epsilon_c(\mathbf{k})$ ($\epsilon_v(\mathbf{k})$).

The effect of QP corrections at the GW level is to blueshift the LDA spectrum. The spectra are dominated by van Hove singularities. The onset of (the real part of) the in-plane G_0W_0 conductivity $\sigma_{xx,yy}(\omega)$ near 1.7 eV is in correspondence with the transitions at the fundamental gap near Γ. The line shape is due to a M_0 critical point of the joint density of states (JDOS) at Γ formed by the two lowest band pairs, to the $1/\omega$ factor present in the relation between conductivity and dielectric function, and to the strong oscillator strength of the corresponding transitions. The second peak at higher energies near 5.5 eV is mainly due to transitions near the *M* **k**-point into the two lowest band combinations. Their flatness [see Fig. 3(e)] gives rise to a strong JDOS and then to a strong optical signature. The next strong spectral feature in the range of 7 eV is related to the next interband combinations near the *M* and *K* points. The inclusion of excitonic effects partially moves back (toward lower energy) the optical absorption edge and the absorption peaks. A strong bound band-edge exciton with binding energy as high as 0.55 eV appears at a photon energy of $\hbar\omega = 1.17$ eV for in-plane light polarization. A second bound exciton peak is visible at $\hbar\omega = 3.9$ eV. It mainly belongs to interband transitions in the QP band structures between the *M* and *K* points of the BZ where the bands are parallel. It is resonant with the continuum of optical transitions at lower energies around the Γ point (see independent-QP spectrum). The binding energy of the corresponding excitons is about 2 eV. The imaginary parts of the in-plane conductivity

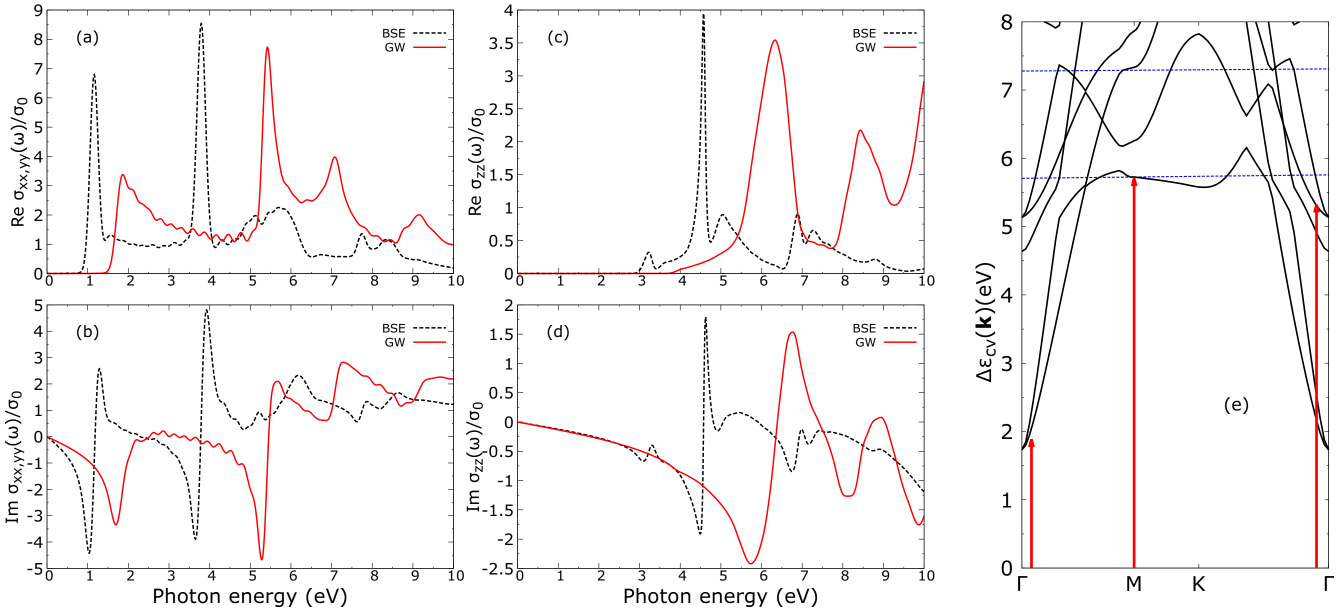

FIG. 3. Real (a), (c) and imaginary part (b), (d) of optical conductivity for *g*-InN calculated with (BSE-black dotted lines) and without (GW-red solid lines) exciton effects for light polarization in-plane (a), (b) and out-of-plane (c), (d). The spectra are normalized to the dc quantum conductivity $\sigma_0 = \frac{e^2}{4\hbar}$ of (the real part of) the in-plane conductivity. Panel (e) displays the G_0W_0 interband structure. The red vertical arrows indicate pronounced interband transitions. The two horizontal blue-dashed lines indicate the position of the first two strong peaks in the JDOS.

look similar as the first derivative of the line shape of the real parts, indicating a pronounced oscillator character of the underlying electron-hole pair excitations. At least for low photon energies, this fact is underlined by the strong and isolated excitonic peaks at 1.2 and 3.9 eV, discussed above, which indeed behave like $1/(\mathrm{E}_{\mathrm{ex}}\text{-}\hbar\omega\text{-i}\Gamma_{\mathrm{ex}})$ in both the imaginary and real parts of the in-plane optical conductivity.

The 1.17 eV excitation energy of the band-edge exciton in Fig. 3(a) is much lower than the 1.90 eV of the electron-hole pairs with binding energy of 0.12 eV in Ref. [27]. This discrepancy is probably due to the self-consistent treatment of the Green's function G in the GW_0 approximation in Ref. [27], because self-consistency tends toward larger gap energies. In addition, the inclusion of the artificial Coulomb interaction between the monolayers in the supercell approach in the VASP code tends to nonconverged results for the QP gap and for the exciton binding energy [53]. A further but smaller effect on the different binding energies may be due to the use of a slightly different lattice constant in the DFT calculations. This also influences the gap to which we are referring the exciton peak, and hence the exciton binding energy.

The optical spectra for the out-of-plane light polarization in Figs. 3(c) and 3(d) are very interesting for the description of light-matter interaction in the case of nonnormal incidence. These spectra show a blueshift of the absorption spectra compared to the excitations in Figs. 3(a) and 3(b) calculated for in-plane polarization. This is a general tendency found for optical spectra of low-dimensional systems [54,55] and is due to strong local-field effects deriving from the strong inhomogeneity of the system along the normal direction. The out-of-plane spectra possess onsets about 2 eV higher in energies due to local-field effects and, especially, allowed optical transitions in the third interband combination near Γ. Bound excitons appear near 3 eV, while pronounced resonant excitations appear somewhat above 4 eV. Therefore, we expect a significant modification of optical spectra of layered systems, including InN sheets for grazing incidence and *p*-polarized light.

We compare these accurate *ab initio* results for the electron-hole pair excitations with what we derived using a simple analytical model for band edge excitons in 2D systems as described in Ref. [49]. Using a variational approach for the model Hamiltonian of excitons in 2D systems, a prediction for the binding energy $\mathrm{E}_b^{\mathrm{exc}}$ and excitonic radius r_{exc} of the first bound exciton can be found. This model requires only the 2D sheet polarizability $\alpha_{2D} = 4.14$ Å and the value of the reduced exciton effective mass $\mu = 0.07\ m$, both achievable from *ab initio* DFT calculations. The sheet polarizability $\alpha_{2D} = (\epsilon_1(0) - 1)L/4\pi$ is computed from the IPA dielectric function of the superlattice for in-plane polarization in the limit of vanishing frequencies and vanishing wave vectors [49]. L is the distance, along the z direction, between two adjacent supercells. Interestingly, this simple model predicts an exciton binding energy of $\mathrm{E}_b^{\mathrm{exc}} = 0.5$ eV (Table III), in very good agreement with the result found from the BSE calculations of 0.55 eV. The large binding energy of excitons suggests the applicability of InN nanosheets embedded in 2D systems with larger gaps (for example GaN) as promising materials for polariton lasers.

V. BILAYER (b-InN)

We explore the geometric properties of InN bilayer within the LDA approach. A similar analysis is also performed within the PBE XC functional, taking into account vdW interaction (PBE+vdW) between the two layers. We investigate the most

TABLE II. Interlayer spacings D and binding energies (with respect to two isolated monolayers) of bilayer stackings. Also electronic gaps calculated at the LDA and LDA+U level are reported.

Stacking	D (Å)	E_{bind} (meV/Å^2)	E_{gap} (LDA) (eV)	E_{gap} (LDA+U) (eV)
AA’	2.40	78.83	0.47	1.34
AA	4.02	4.58	0.45	1.27
AB In on In	3.53	10.55	0.43	1.25
AB In on N	2.71	35.05	0.22	0.99

stable stacking sequence comparing the total energy of the bilayer configurations: (1) AA’ stacking sequence, in which we have hexagons on top of each other, with the In atom being above N, (2) AA stacking with In on In, (3) AB Bernal type configuration with In above N, and (4) AB’ Bernal type configuration with In on In. The difference in total energy between two isolated g-InN and the b-InN characterizes the binding energy between the two monolayers. This is listed in Table II and demonstrate that the AA’ sequence is energetically most favorable. This can be understood by noticing that b-InN in the AA’ stacking represents a building block toward the WZ InN bulk structure. The largest energy gain is not only due to the vdW attraction of the two layers but also to the overlap of the p_z valence orbitals of In and N, leading to a weak vertical chemical bond. The energy gain for AA’ in Table II suggests that experimentally it will be easier to grow bilayers than monolayers because of the additional stabilization due to the layer binding energy $E_{\rm bind}$ of the order of 80 meV/Å^2. The others stackings AA, AB (In on In), and AB (In on N) gain less energy. As a consequence, we find the smallest layer distance of the two InN monolayers for AA’ among the stackings considered.

Using the LDA (PBE+vdW) framework, we have calculated the lateral lattice constant $a = 3.63$ Å (3.73 Å), the interlayer spacing $D = 2.40$ Å (2.54 Å), and the in-plane bond length $d = 2.09$ Å (2.16 Å) for the equilibrium AA’ sequence. The in-plane bonding in each InN layer is weakened compared to the monolayer case ($d = 2.03$ Å). The weaker intralayer spacing originates from the additional mixed ionic-covalent In-N bonds in the stacking direction. Comparing the geometric characteristics obtained for two different XC functionals, we can say that the LDA gives reasonable results, in particular for the interlayer distance.

TABLE III. Isotropic effective masses m_e^* and m_h^* of electrons and holes from Kohn-Sham bands around the Γ point. Results within the 2D excitonic model [49] are also listed: excitonic binding energy $E_b^{\rm exc}$ and excitonic radius $r_{\rm exc}$. The model optical gaps (calculated as $E_{\rm gap}$(LDA+U)- $E_b^{\rm exc}$) for the different stacking sequences of InN bilayer and for monolayer g-InN are also shown.

	m_e^* (m)	m_h^* (m)	α_{2D} (Å)	$E_{\rm gap}^{\rm opt}$ (eV)	$E_b^{\rm exc}$ (eV)	$r_{\rm exc}$ (Å)
AA’	0.048	0.98	8.87	1.08	0.26	30.0
AA	0.049	0.75	9.79	1.03	0.24	31.5
AB In on In	0.051	0.86	10.17	1.0	0.25	31.2
AB In on N	0.040	0.85	15.57	0.82	0.17	39.4
g-InN	0.083	0.43	4.14	1.14	0.50	17.2

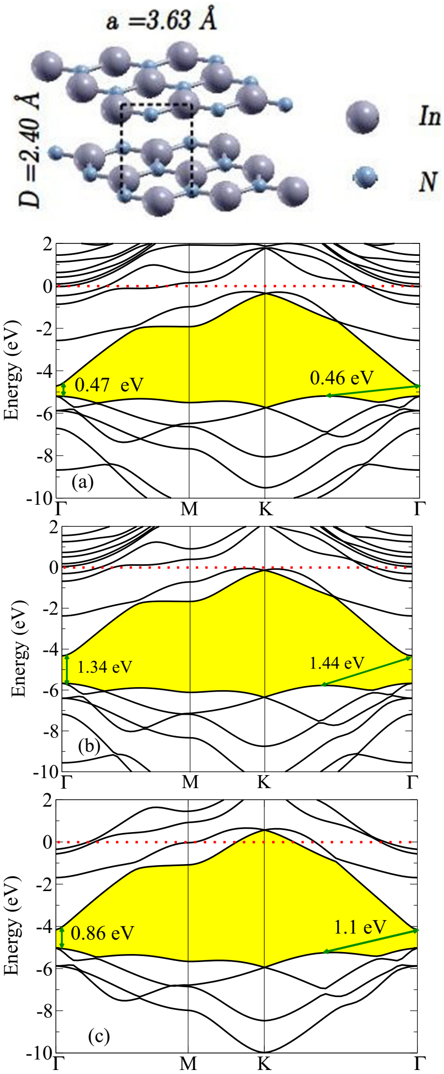

FIG. 4. The optimized hexagonal atomic structure of b-InN in the more stable AA’ stacking sequence. The lattice constant a and the interlayer distance D are indicated. Large (grey) and small (blue) balls denote In and N atoms, respectively. Band structure of b-InN within LDA (a), LDA+U (b), and GW approximation (c). The vacuum level, identified with the energy zero, is displayed as a red dotted horizontal line.

The electronic band structures of the most stable AA’ stacking of b-InN, calculated along the high-symmetry lines $\Gamma \rightarrow M \rightarrow K \rightarrow \Gamma$, are presented in Fig. 4. On first glance, the band structures are very similar to those for the monolayer. The vertical doubling of the unit cell and, hence, the number of atoms, give rise to a doubling of the number of bands. They are, however, not degenerate due to the electronic interactions across the interface between the two monolayers, e.g., the mutual increase of the screening by image potential effects. We obtain a LDA direct gap at Γ of 0.46 eV quasidegenerate with the indirect gap of 0.47 eV. For the indirect gap, the VBM occurs at $\mathbf{k}^* = (0.4, 0)2\pi/a$ at the $K\Gamma$ line, while the

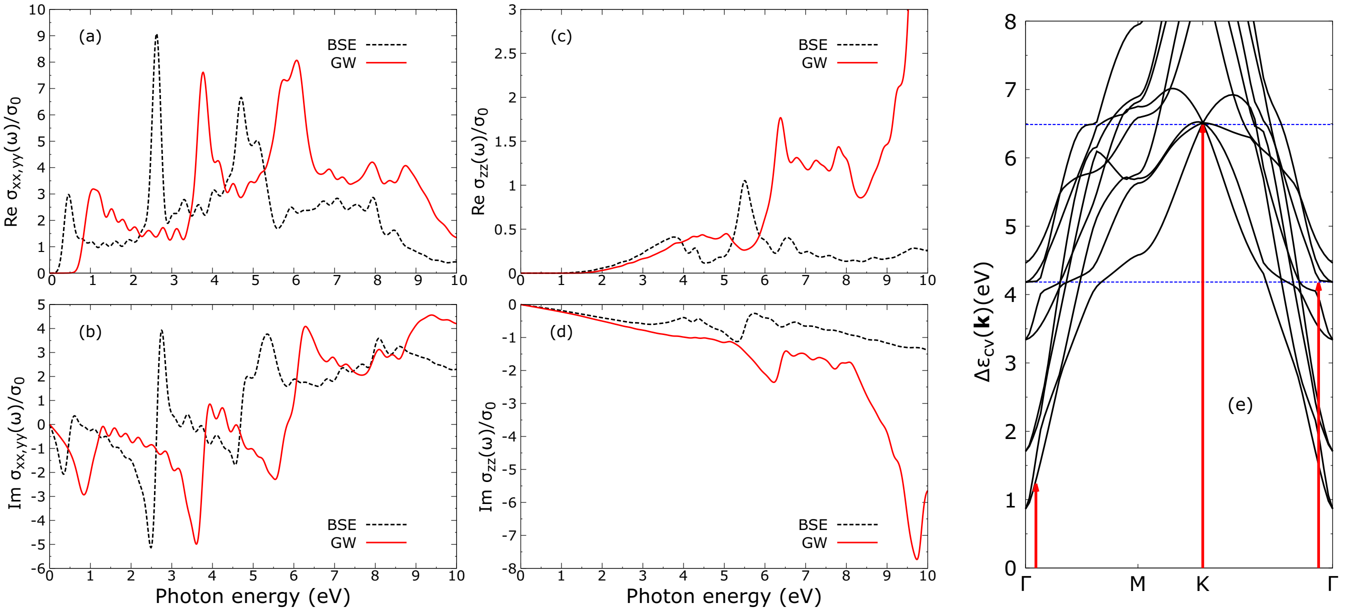

FIG. 5. Real (a) and imaginary part (b) of optical conductivity for *b*-InN calculated with (BSE-black dashed lines) and without (GW-red solid lines) exciton effects for light polarization in-plane (a), (b) and out-of-plane (c), (d). The spectra are normalized to the dc quantum conductivity $\sigma_0 = \frac{e^2}{4\hbar}$. Panel (e) displays the G_0W_0 interband structure. The red vertical arrows indicate pronounced interband transitions. The two horizontal blue-dashed lines indicate the position of the first two strong peaks in the JDOS.

lowest unoccupied level appears at Γ. As for *g*-InN, no band inversion occurs.

Since the LDA+U approach has been shown to be a reasonable approximation both for bulk and for *g*-InN, we have performed a LDA+U calculation also for the AA' *b*-InN. The resulting gap in Fig. 4(b) is direct, at Γ, and amounts to 1.34 eV. The indirect gap $\mathbf{k}^*\Gamma$ turns out to be 1.44 eV.

Using the G_0W_0 approximation to calculate the accurate electronic structure, shown in Fig. 4(c), we obtain a direct Γ-Γ gap of 0.86 eV (see Table I) and an indirect $\boldsymbol{k}^*\Gamma$ gap of 1.1 eV. As for *g*-InN, by applying the G_0W_0 corrections to the electronic structure, the almost degeneracy of the two gaps disappears completely.

Comparing the GW gaps with those obtained within LDA+U we can affirm that, in contrast to *g*-InN, for *b*-InN the agreement is only qualitative. In both cases, a direct gap semiconductor is obtained but, from a quantitative point of view, the LDA+U approximation overestimates the gaps, probably, by overestimating the confinement effects in the bilayer case. As expected, the fundamental band gap decreases going from monolayer to bilayer due to the minor confinement and larger screening effects in the direction perpendicular to the layer. There is a tendency to approach the bulk gap value with an increasing number of monolayers. However, this tendency is not monotonous.

In Table II, the gaps for the other stacking sequences studied within the LDA and LDA+U approaches are listed. For the AB Bernal type stacking sequence with the indium atoms on top of nitrogen, we registered a LDA energy gap smaller than 50% compared to other configurations. Consequently, the LDA+U gap also has a lower value. The stacking influences the actual gap value. The bilayer AA' system is characterized by an ionization energy $I = 5.03$ eV (5.67 eV, 5.12 eV) and an electron affinity $A = 4.17$ eV (4.33 eV, 4.65 eV) within the LDA+G_0W_0 (LDA+U, LDA) approximation. These values are not too different from electron affinity and ionization energy of *g*-InN. While in LDA and LDA+U A and I are practically independent of the number of layers, within the GW QP approximation such dependence is restored, due to the dimensionality-dependent reduced confinement and screening.

In Fig. 5, the *ab initio* polarization-dependent optical conductivities with and without excitonic effects calculated within the BSE approach are shown. As for *g*-InN, the inclusion of the electron-hole interaction shifts all spectra toward lower energy. The first absorption peak of *b*-InN and normal incidence in Fig. 5(a) is at 0.42 eV and indicates a binding energy for the first bound exciton of $E_b^{\mathrm{exc}} = 0.44$ eV, slightly less than the binding energy of *g*-InN but still much higher than that of the bulk structure (around 5 meV [34]). It is due to optical transitions into the two lowest interband combinations near Γ [see Fig. 5(e)]. A second peak appears at 2.6 eV. It belongs to transition also near Γ but into the fifth and sixth band pairs and is resonant with the continuum of lowest $\Gamma - \Gamma$ transitions. The peak around 4.5 eV originates from transitions between several interband combinations near the *K* point. Interestingly, the out-of-plane polarization absorption in Fig. 5(c) does not show band edge excitons, indicating, on the first view, seemingly a saddle-point behavior of the underlying van Hove singularity in the region 1–4 eV related to higher valence bands and lower conduction bands at Γ [see Fig. 5(e)]. However, in Fig. 5(e), the band pairs at Γ show an M_0 van Hove character. Thereby, the seventh and eighth band pairs show a vanishing dispersion near Γ, giving rise to a strong peak in the joint density of states (JDOS) but not in the independent-QP spectrum. This observation may be related to vanishing optical matrix elements for the in-plane light polarization.

Since the 2D excitonic model results for group-IV 2D honeycomb sheets [49] and for *g*-InN agree very well with those obtained by the *ab initio* BSE treatment, we use the model calculations to evaluate the exciton binding energy and radius for the different stacking sequences of *b*-InN. We note that for the AB In on N stacking (see Table III) the exciton binding energy is smaller than the AB In on In and AA, AA' sequences. Consequently, the excitonic radius is larger. The 2D exciton model clearly explains why in bilayer InN the exciton binding is reduced compared to the monolayer case. As a consequence of the smaller gap, the very small effective mass of the electrons is significantly reduced going from 1 ML to the bilayer (see Table III). Simultaneously, the value α_{2D} of the static polarizability is increased because increased screening in the presence of a second atomic layer. Both effects together explain the reduction of the exciton binding and the increase of the in-plane exciton radius by a factor of 2 going from *g*-InN to *b*-InN.

Comparing the full *ab initio* result for the binding energy (Table I) with that of the model (Table III), which means 0.44 eV versus 0.26 eV, we note a severe underestimation of binding energy by the latter compared to the case of the monolayer. This is due to the fact that this model is suitable for the study of excitons in 2D systems with vanishing thickness. In two-layer systems, the 2D limit is less fulfilled.

VI. SUMMARY AND CONCLUSIONS

We have presented a theoretical analysis of InN structures from bulk to bilayer and to graphenelike single layer. We studied bulk WZ and ZB structures within the LDA+U approximation to improve the description of the DFT band structures of the 3D InN. We found that applying the Hubbard U correction to both *p* states of nitrogen and *d* states of indium, we recover the correct symmetry and ordering of the energy levels at the Γ point of Brillouin zone. For nanoscale InN we have calculated the band structures within LDA but also applied LDA+U and GW corrections. In particular, for *g*-InN the $\Gamma - \Gamma$ direct LDA+U gap of 1.64 eV is close to the many-body GW $\Gamma - \Gamma$ direct gap of 1.72 eV. We found that the AA' bilayer structure is the most stable stacking sequence in the bilayer case. We obtain a DFT-LDA direct gap at Γ of 0.47 eV that increases until 1.34 eV with the application of the Hubbard U correction, while within the G_0W_0 approximation we obtain a $\Gamma - \Gamma$ direct gap of 0.86 eV. We found that going from one monolayer to the bilayer, the electronic gap almost halves and remains direct.

By solving the BSE, we obtained the optical spectra of *g*-InN and *b*-InN. Their absorption edges for in-plane light polarization are characterized, respectively, by a peak at 1.17 eV and 0.42 eV of the lowest-bound electron-hole pairs. There is a tendency that the QP effects and exciton binding energy compensate each other. For out-of-plane light polarization, the absorption edges are blueshifted, indicating a significant influence of light polarization and propagation in the blue and UV spectral ranges. Finally, we predict extremely small effective masses for the electrons in the bilayer, independently of the stacking, thus suggesting that *b*-InN could be a precious building block for fast low-dimensional nanoelectronic devices.

ACKNOWLEDGMENTS

EU HORIZON2020 funding through the MSC RISE CoExAN (GA644076) is acknowledged. F.B. gratefully thanks INFN Tor Vergata for travel support. CPU time was granted by CINECA and CRESCO HPC centers.

[1] J. E. Moore, Nat. **464**, 194 (2010).

[2] C. Cervetti, A. Rettori, M. G. Pini, A. Cornia, A. Repollés, F. Luis, M. Dressel, S. Rauschenbach, K. Kern, M. Burghard *et al.*, Nat. Mat. **15**, 164 (2016).

[3] L. Tao, E. Cinquanta, D. Chiappe, C. Grazianetti, M. Fanciulli, M. Dubey, A. Molle, and D. Akinwande, Nat. Nanotech. **10**, 227 (2015).

[4] Y. Saito, T. Nojima, and Y. Iwasa, Nat. Rev. Mater. **2**, 16094 (2016).

[5] D. A. Steigerwald, J. C. Bhat, D. Collins, R. M. Fletcher, M. O. Holcomb, M. J. Ludowise, P. S. Martin, and S. L. Rudaz, IEEE J. Sel. Top. Quantum Electron. **8**, 2, 310 (2002).

[6] S. R. Routray and T. R. Lenka, CSI Transactions on ICT. **6**, 83 (2018).

[7] C. R. Woods, L. Britnell, A. Eckmann, R. S. Ma, J. C. Lu, H. M. Guo, X. Lin, G. L. Yu, Y. Cao, R. V. Gorbachev, A. V. Kretinin, J. Park, L. A. Ponomarenko, M. I. Katsnelson, Yu. N. Gornostyrev, K. Watanabe, T. Taniguchi, C. Casiraghi, H-J. Gao, A. K. Geim, and K. S. Novoselov, Nat. Phys. **10**, 451 (2014).

[8] P. Tsipas, S. Kassavetis, D. Tsoutsou, E. Xenogiannopoulou, E. Golias, S. A. Giamini, C. Grazianetti, D. Chiappe, A. Molle, M. Fanciulli, and A. Dimoulas, Appl. Phys. Lett. **103**, 251605 (2013).

[9] S. Alamiè, A. N. Quezada, D. Skuridina, C. Reich, D. Henning, M. Frentrup, T. Wernicke, I. Koslow, M. Kneissl, N. Esser, and P. Vogt, Mater. Sci. Semicon. Proc. **55**, 7 (2016).

[10] A. Onen, D. Kecik, E. Durgun, and S. Ciraci, Phys. Rev. B **93**, 085431 (2016).

[11] M. S. Prete, A. Mosca Conte, P. Gori, F. Bechstedt, and O. Pulci, Appl. Phys. Lett. **110**, 012103 (2017).

[12] D. Kecik, A. Onen, M. Konuk1, E. Gürbüz, F. Ersan, S. Cahangirov, E. Aktürk, E. Durgun, and S. Ciraci, Appl. Phys. Rev. **5**, 011105 (2018).

[13] N. Sanders, D. Bayerl, G. Shi, K. A. Mengle, and E. Kioupakis, Nano Lett. **17**, 7345 (2017).

[14] D. Bayerl, S. M. Islam, C. M. Jones, V. Protasenko, D. Jena, and E. Kiopakis, Appl. Phys. Lett. **109**, 241102 (2016).

[15] Z. Y. A. Balushi, K. Wang, R. K. Ghosh, R. A. Vilá, S. M. Eichfeld, J. D. Caldwell, X. Qin, Y.-C. Lin, P. A. De Sario, G. Stone *et al.*, Nat. Mater. **15**, 1166 (2016)

[16] J. Liao, B. Sa, J. Zhou, R. Ahuja, and Z. Sun, J. Phys. Chem. C **118**, 17594 (2014).

[17] J. M. Phillips, M. E. Coltrin, M. H. Crawford, A. J. Fischer, M. R. Krames, R. Muller-Mach, G. O. Mueller, Y. Ohno, L. E. S. Rohwer, J. A. Simmons, and J. Y. Tsao, Laser & Photon. Rev. **1**, 307 (2007).

[18] L. C. de Carvalho, A. Schleife, J. Furthmuller, and F. Bechstedt, Phys. Rev. B **85**, 115121 (2012).

[19] V. Yu. Davydov, A. A. Klochikhin, R. P. Seisyan, V. V. Emtsev, S. V. Ivanov, F. Bechstedt, J. F. Üller, H. Harima, A. V. Mudryi, J. Aderhold, O. Semchinova, and J. Graul, Phys. Status Solidi B **229**, R1 (2002).

[20] L. C. de Carvalho, A. Schleife, and F. Bechstedt, Phys. Rev. B **84**, 195105 (2011).

[21] J. Kuzmík, Semicon. Science & Technol. **29**, 035015 (2014).

[22] T.-T. Kang, X. Liu, R. Q. Zhang, W. G. Hu, G. Cong, F.-A. Zhao, and Q. Zhu, Appl. Phys. Lett. **89**, 071113 (2006).

[23] H. Y. Xu, Z. Liu, X. T. Zhang, and S. K. Hark, Appl. Phys. Lett. **90**, 113105 (2007).

[24] X. P. Chen, N. Yang, J. M. Ni, M. Cai, H. Y. Ye, C. K. Wong, S. Y. Leung, and T. L. Ren, IEEE Electron Device Lett. **36**, 1366 (2015).

[25] C. E. Villegas, A. R. Rocha, J. Phys. Chem. C, **119**, 11886 (2015).

[26] H. Sahin, S. Cahangirov, M. Topsakal, E. Bekaroglu, E. Akturk, and R. T. Senger, S. Ciraci Phys. Rev. B **80**, 155453 (2009).

[27] D. Liang, R. Quhe, Y. Chen, L. Wu, Q. Wang, P. Guan, S. Wang, and P. Lu, RSC Adv. **7**, 42455 (2017).

[28] V. Wang, Z. Q. Wu, Y. Kawazoe, and W. T. Geng, J. Phys. Chem. C **122**, 6930 (2018).

[29] X. Sun, Q. Yang, R. Meng, C. Tan, Q. Liang, J. Jiang, H. Ye, and X. Chen, App. Surf. Sci. **404**, 291 (2017).

[30] F. Bechstedt and J. Furthmüller, J. Cryst. Growth **246**, 315 (2002).

[31] P. Hohenberg and W. Kohn, Phys. Rev. **136**, B864 (1964).

[32] W. Kohn and L. J. Sham, Phys. Rev. **140**, A1133 (1965).

[33] D. Vogel, P. Krüger, and J. Pollmann, Phys. Rev. B **55**, 12836 (1997).

[34] F. Fuchs, C. Rödl, A. Schleife, and F. Bechstedt, Phys. Rev. B **78**, 085103 (2008).

[35] L. F. J. Piper, T. D. Veal, P. H. Jefferson, C. F. McConville, F. Fuchs, J. Furthmuller, F. Bechstedt, Hai Lu, and W. J. Schaff, Phys. Rev. B **72**, 245319 (2005).

[36] http://www.quantum-espresso.org.

[37] A. F. Wright and J. S. Nelson, Phys. Rev. B **51**, 7866 (1995).

[38] J. P. Perdew, K. Burke, and M. Ernzerhof, Phys. Rev. Lett. **77**, 3865 (1996).

[39] M. Dion, H. Rydberg, E. Schroder, D. C. Langreth, and B. I. Lundqvist, Phys. Rev. Lett. **92**, 246401 (2004).

[40] F. Bechstedt, *Many-Body Approach to Electronic Excitations*, (Springer, Berlin, 2016).

[41] J. Furthmuller, P. H. Hahn, F. Fuchs, and F. Bechstedt, Phys. Rev. B **72**, 205106 (2005).

[42] See www.etsf.eu for the GW code CHISIG developed within the ETSF.

[43] C. A. Rozzi, D. Varsano, A. Marini, and E. K. U. Gross A. Rubio, Phys. Rev. B **73**, 205119 (2006).

[44] M. Rohlfing and S. G. Louie, Phys. Rev. B **62**, 4927 (2000).

[45] O. Pulci, P. Gori, M. Marsili, V. Garbuio, R. Del Sole, and F. Bechstedt, Europhys. Lett. **98**, 37004 (2012).

[46] http://etsf.polytechnique.fr/exc.

[47] L. V. Keldysh, JETP Lett. **29**, 658 (1979).

[48] R. R. Guseinov, Phys. Status Solidi B, **125**, 237 (1984).

[49] O. Pulci, M. Marsili, V. Garbuio, P. Gori, I. Kupchak, F. Bechstedt, Phys. Status Solidi B **252**, 72 (2015).

[50] A. Terentjevs, A. Catellani, D. Prendergast, and G. Cicero, Phys. Rev. B **82**, 165307 (2010).

[51] J. Heyd, G. E. Scuseria, and M. Ernzerhof, J. Chem. Phys. **118**, 8207 (2003).

[52] P. Yu and M. Cardona, *Fundamentals of Semiconductors: Physics and Materials Properties* (Springer, Berlin, 1996).

[53] L. Wirtz, A. Marini, and A. Rubio, Phys. Rev. Lett. **96**, 126104 (2006).

[54] A. G. Marinopoulos, L. Reining, A. Rubio, and N. Vast, Phys. Rev. Lett. **91**, 046402 (2003).

[55] L. Matthes, O. Pulci, and F. Bechstedt, Phys. Rev. B **94**, 205408 (2016).